

Investigation of Image Formation with Coherent Illumination in Deep Turbulence

R. Holmes

Boeing LTS, 4411 The 25 Way, Suite 350, Albuquerque, NM 87109

V. S. Rao Gudimetla

Air Force Research Laboratory, 550 Lipoa Parkway, Kihei, HI 96753

ABSTRACT

Image formation with coherent active illumination poses special difficulties due to the presence of laser speckle in a coherent image. Such laser speckle is similar to atmospheric speckle and so is difficult to separate from the latter in the focal plane. On the other hand, it can be proven that atmospheric phase and laser speckle can be separated in the pupil plane when atmospheric turbulence is concentrated at the receiver. A wave-optics simulation is used to form images and test various image reconstruction algorithms for isolated, actively-illuminated objects. The most successful algorithms tested so far in deep turbulence involve blind iterative deconvolution in the focal plane and branch-cut estimation in the pupil plane. Significant improvements can be found for spherical-wave log-amplitude variances up to 0.4, for uniform-turbulence scenarios over a 30 km range. For such cases there are 10 atmospheric coherence lengths (r_0) across the aperture, one isoplanatic patch per diffraction angle (λ/D), and 20 or more isoplanatic patches across the object. Most of the image quality is typically obtained with about eight frames of raw data. The results are assessed using several image metrics and compared with a corresponding idealized adaptive-optics approach using a point-source incoherent beacon.

1.0 INTRODUCTION

Image formation based on coherent illumination of an object can aid in improving signal from dim objects in known areas of interest. However, the reflected light is known to exhibit laser speckle [1-3]. Such coherent speckle is often considered a source of noise in both the radar and optical domains. On the other hand, the coherent speckle field can provide useful information about an object. This information has been exploited in the optical domain in the past, in which coherent laser speckle is sampled in the pupil plane and digitally propagated to the image plane. Examples include various forms of holography, including film-based holography [4], digital holography [5-9], digital holography with Hartmann wavefront sensors [10], and two-speckle-field holography [11]. In the focal plane, it is known that it is especially difficult to form images when both atmospheric speckle and laser speckle are present [12]. Many techniques have been developed to suppress the effects of laser speckle in imagery [13-16].

Atmospheric turbulence is known to cause degradation of image quality, especially at wavelengths in the visible or near-infrared [17-22]. Radar operating at longer wavelengths can be insensitive to such degradations [23]. Formation of high-quality radar images typically involves synthetic-aperture approaches that require transmission of many coherent pulses [2]. Because of these considerations, one seeks an active imaging approach that can form images requiring just a few time samples of image data, and which can reconstruct images quickly.

This paper considers several straightforward modalities for such “snapshot” imagery. Related imaging modalities considered for this application in the past include the use of adaptive optics (AO) [20-22, 24-25], the pupil-plane approaches mentioned above, and various approaches that exploit the properties of laser speckle in the focal plane [26-38]. One intent of this effort is to extend these approaches to pupil-plane and focal-plane data wherein the measurements are *not* performed via heterodyne detection.

With active imaging, there are several time scales of significance. These include the time duration of a coherent pulse, and the time scale over which the reflected coherent speckle (laser speckle) changes. The latter is important in

this case in order to obtain the pupil-plane laser speckle from which the object is reconstructed [3]. The time constant over which the illuminator-induced speckle field in the pupil decorrelates by 50% will be referred to as the coherent speckle time constant. In this paper, the assumed imaging conditions are (a) pulse durations much shorter than the atmospheric time constant and the coherent speckle time constant, (b) detector sample durations much shorter than both the atmospheric time constant and coherent speckle time constant, and (c) durations between samples much longer than the atmospheric time constant coherent speckle time constant.

Because the imaging considered in this paper involves active illumination, only high-SNR conditions will initially be considered. Later papers will consider low-SNR conditions. Another idealization is that high spatial resolution is assumed for pupil-plane approaches, with 4 mm sampling of the pupil. A last idealization is that it is assumed that the target is uniformly illuminated. Furthermore, the presence of branch points of the phase in the pupil plane due to strong turbulence can present a challenge for reconstruction of the phase of laser speckle. Deep turbulence is defined herein as when the scintillation index for a spherical wave exceeds 0.4. This corresponds to a spherical wave log-amplitude (SWLA) variance σ_R^2 of 0.1 using the relation $\sigma_I^2 = \exp(4\sigma_R^2) - 1 \approx 4\sigma_R^2$ where σ_I^2 is the scintillation index. Note that plane-wave values for scintillation index and log-amplitude variance are 2.5x larger than for spherical waves. Thus the threshold value is a fixed fraction of the definition of strong turbulence in the literature, which corresponds to a scintillation index of 1 or more for a plane wave [19, p. 324]. Moderate turbulence will arbitrarily be defined in this paper as cases in which the SWLA variance is in the range of 0.1 to 0.25. Similarly, weak turbulence is defined to correspond to a value of less than 0.1.

This paper discusses and compares both focal plane and pupil plane approaches with non-heterodyne measurement processes. As an example of the latter, a Hartmann-Shack wavefront sensor at high spatial resolution can provide such non-heterodyne measurements of pupil-plane data. Other non-heterodyne approaches that measure the phase differences and intensity in the pupil plane include use of a self-referencing interferometer.

A relatively simple pupil-plane image reconstruction algorithm was recently considered [29], using an analytic approach. This approach, related to that of [30], uses the fact that for turbulence concentrated at the receiver the measured pupil-plane field is the product of the laser speckle field and an atmospheric phasor:

$$E_{\text{pupil}}(\mathbf{x}) = (i/\lambda R) \exp[i\phi_{\text{atm}}(\mathbf{x})] \int E(\mathbf{x}') \exp[i(k_0/2R)|\mathbf{x}-\mathbf{x}'|^2] d\mathbf{x}' \quad (1)$$

where $E_{\text{pupil}}(\mathbf{x})$ is the electric field measured in the pupil, $\phi_{\text{atm}}(\mathbf{x})$ is the phase arising from atmospheric turbulence, $E(\mathbf{x}')$ is the reflected electric field at the object plane, $k_0 = 2\pi n/\lambda$ is the optical wavenumber in air, λ is the optical wavelength, n is the refractive index at that wavelength, and R is the path length. Because of the rapid and large variations of the phase of the reflected field in the object plane upon reflection from the (assumed rough) surface of the object, the term $\exp[i(k_0/2R)|\mathbf{x}'|^2]$ can be neglected. Then writing out Eq. (1) assuming equally-spaced discrete measurement samples in the object plane, one has

$$E_{\text{pupil}}(z_x, z_y) = C F(z_x, z_y) \sum_{n_x, n_y} E(n_x, n_y) \quad (2)$$

where $z_x(x) = \exp(i(k_0/R)x\Delta x')$, $z_y(y) = \exp(i(k_0/R)y\Delta y')$, $C = [i\Delta x'\Delta y' / (\lambda R)] E_0$, and $F(z_x, z_y) = \exp[i\phi_a(\mathbf{x})] \exp[i(k_0/R)|\mathbf{x}'|^2]$. $\Delta x'$ and $\Delta y'$ are the selected spacing in the object plane, chosen based on Nyquist sampling given the receiver diameter, object range, and imaging wavelength. Note that written in this form, E_{pupil} is the product of an analytic function in each of the two variables z_x and z_y , multiplied by an atmospheric phasor function. The latter is not in general an analytic function of these variables. In this special case of turbulence near the receiver, the atmospheric phasor function $F(z_x, z_y)$ has no zeroes, and so all zeroes therefore belong to the speckle field. This special case is investigated below,

and will be found to work in relatively weak turbulence (as measured by spherical-wave log-amplitude variance) in the scenarios considered.

To address turbulence with greater scintillation, including those with branch points, other approaches are considered. One idealized approach is to use an incoherent beacon located at the center of the object to estimate and remove the return from this beacon as an estimate of atmospheric phase. This idealized approach should be an upper bound on any pupil-plane imaging modality using a single beacon. This approach will be referred to as “Point Source Phase Removed” (PSPR) in the following. This approach can be realized with adaptive optics for weak turbulence, and alternatively via the obvious post-processing approach in all turbulence regimes. Results for this approach are shown below.

Several other approaches are considered to separate the speckle field from the atmospheric phase in Eq. (1) or the stronger-turbulence versions of the equation. First, one might associate the irrotational phase with the atmospheric phase, and rotational phase with the laser speckle phase. This approach was investigated, but it was found that the laser speckle phase has a significant irrotational part. Sample results are shown below. A second alternative is to separate the atmospheric phase from the laser speckle phase according to their spatial statistics, which are quite different. It was found that the most straightforward form of statistical filtering, though optimal in some sense, executed very slowly and did not converge to the correct phase in many cases. These issues could be associated with the implementation. Regardless, this second alternative was also not pursued further.

Another approach to statistical filtering to separate the laser speckle from the atmospheric phase is to consider the irrotational phase in the pupil, decompose it into Zernike aberrations, and associate that portion of the Zernike aberration which is within some range of the expected (and assumed known) variance of the aberration due to turbulence. This form of statistical filtering executed quickly and performed relatively well as shown below.

Further, in moderate turbulence, the presence of branch points due to atmospheric turbulence can be addressed by associating the branch points to atmospheric turbulence which have relatively short branch-cut lengths between them. A physical explanation for this choice is that in moderate turbulence, zeroes in the electric field that are formed from atmospheric scintillation do not have an opportunity to migrate far from each other, i.e., the probability that they are close together is relatively large. However, the process of associating branch points of opposite polarity to each other and forming the branch cut is also an art, as indicated in [31-37]. Results for several of these algorithmic variants are also presented in this paper.

In addition to the above pupil-plane algorithms, several fast-running focal-plane algorithms are also considered. First, the well-known Generalized Expectation Maximization (GEM) algorithm is applied using the isoplanatic version [38]. Second, a variant of the single-frame blind iterative deconvolution (BID) algorithm [39] is applied to this problem of active imaging. To address the issues related to coherent imaging in the focal plane, the BID algorithm is modified to filter out the higher spatial frequencies, which is where much of the laser-speckle modulation is known to be located (in the focal plane). This filtering also has the undesirable consequence of filtering out higher spatial frequencies in the object, as well as some part of the atmospheric speckle that can be used to extract object information. However, the benefit of such filtering is found to outweigh the disadvantages for a proper choice of filtering for the cases considered.

To summarize the assumptions and limitations of this paper, the approach considers high-SNR, well-sampled measurements of coherent laser speckle return in the focal plane or pupil plane for horizontal-path scenarios with uniform turbulence along the path and with an emphasis on spherical-wave log-amplitude variances of 0.1 or more. The objects are assumed to be spatially isolated and uniformly illuminated. This initial effort focuses on algorithms that run quickly, are relatively simple to implement, and only require a few frames of data. The latter, just a few frames of data, is motivated by the earlier discussion of the existence proof for separation of laser speckle from atmospheric phase in weaker turbulence with just one frame of data.

Section 2 discusses the scenarios and the approach for simulation of the raw imagery. Section 3 discusses the image reconstruction approaches considered. Section 4 presents results. Section 5 summarizes the effort.

2. SIMULATION APPROACH

Table 1 presents specific inputs and settings used for the wave-optics simulation. The simulation approach is to uniformly illuminate an isolated object (such as an object moving in the air), to apply a complex-Gaussian random amplitude at each grid point, to perform angular filtering of that random field so that the light stays in the propagation grid, and then to propagate the light through a number of phase screens back to a receiver using the usual split-operator technique. At the receiver, a circular aperture mask is applied for pupil-plane imaging. For focal-plane imaging, a focus is applied and the result is propagated to a focal plane where the intensity of the received electromagnetic field is formed.

The resulting data is a single polarization of light returning from the object. Up to 20 images are formed with the steps outlined above. For pupil-plane processing, a beacon source is placed at the center of the object with full-width at half-max of 2 cm. The light is then propagated to the receiver, with 4-mm grid resolution. The grid resolution sets the inner scale. The received beacon field's complex phase is computed in the pupil-plane at the resolution of the grid. This beacon phase is removed from the complex electric field comprising both laser speckle and atmosphere by taking the complex conjugate of the atmospheric phase. It should be noted that these simulations for propagation of laser speckle through turbulence have received significant validation in past efforts [40-42].

Table 1. Simulation input parameters.

Parameter	Value
Propagation Grid Size	1024 x 1024
Grid Point Spacing (mm)	4
Path Length (km)	30
# Phase Screens	10
Wavelength (nm)	1064
# time steps	up to 20
Object(s)	letter "A", others
Type of illumination	Temporally Coherent
Aperture Diameter (m)	1.0
Turbulence Strength	$\sigma_R^2=10^{-4}-1.3$
Turbulence Type	Kolmogorov, 5 meter outer scale
Detector Type – Pupil Plane	Idealized, 4 mm pixels
Detector Type – Focal Plane	Idealized, 133 nrad pixel FOV

The time sampling is set to 0.01 seconds between frames. The atmospheric turbulence and speckle are made completely decorrelated between these frames. This modeling of frozen speckle and turbulence conditions can be achieved in practice with laser pulse durations of a microsecond or less.

Fig. 1 displays the first set of objects considered. These objects comprise three different sizes of the letter "A." This object is of moderate complexity and of bounded (finite) support. Fig. 2 shows a second set of objects considered.

Table 2 shows the corresponding key atmospheric parameters for the cases that were simulated. It should be noted that (a) the receiver aperture of 1-meter diameter is much smaller than the grid size, and (b) that in many cases, the atmospheric turbulence

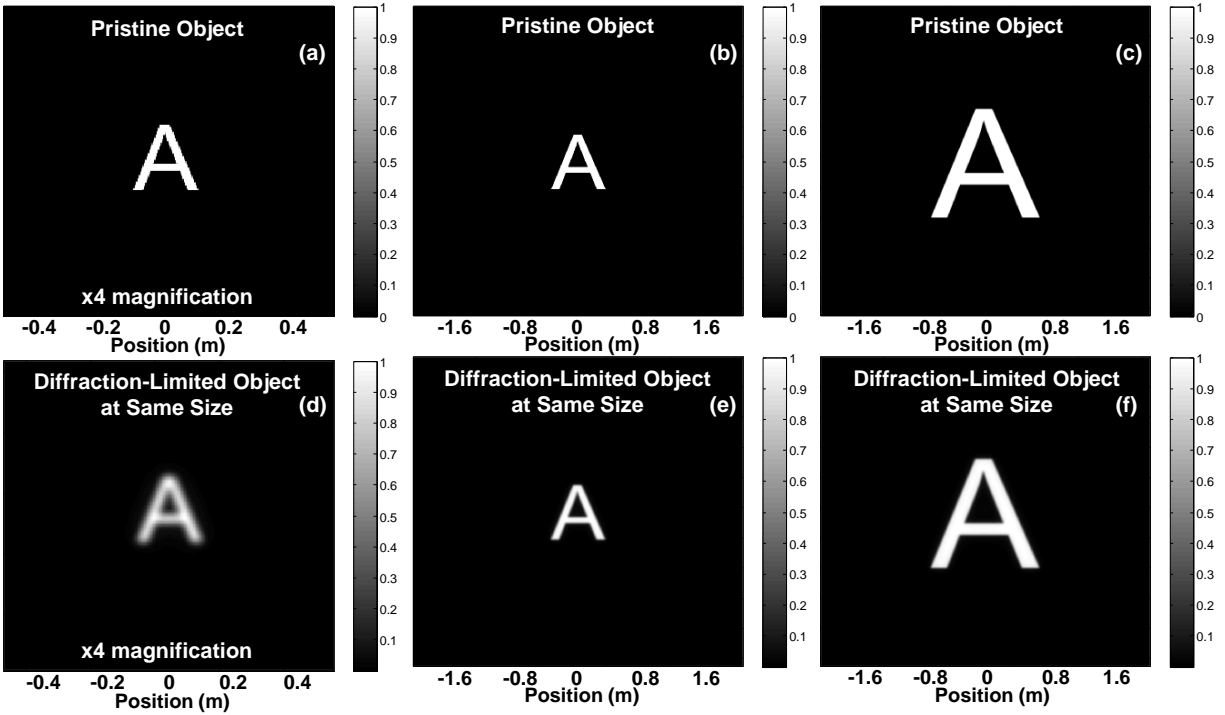


Fig. 1. Pristine and diffraction-limited “A” objects with 1 meter aperture, 30 km range. (a)-(c): Pristine objects of size 21, 80, and 144 cm, respectively. (d)-(f): Diffraction-limited objects of size 21, 80, and 144 cm, respectively

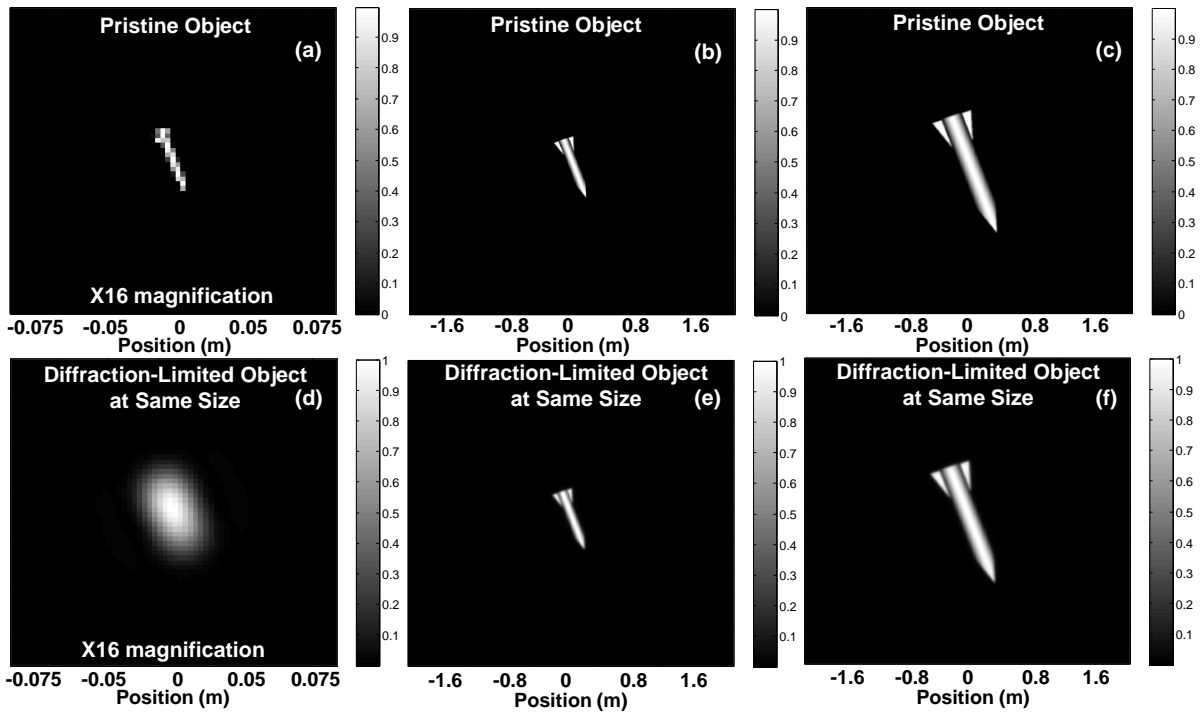


Fig. 2. Pristine and diffraction-limited “missile” objects with 1 meter aperture, 30 km range. (a)-(c): Pristine objects of size 4.8, 80, and 160 cm, respectively. (d)-(f): Diffraction-limited objects of size 4.8, 80, and 160 cm, respectively.

would be considered severe. In particular, for the cases of SWLA variance [43] of 0.3 or higher, the isoplanatic patch angle [44-46] is comparable to or less than the diffraction angle, which is defined as wavelength/(aperture diameter). These cases also have 20 or more isoplanatic patch angles across the object angular subtense for the medium-sized object, and have up to 10 atmospheric coherence lengths [47-48] across the receiver aperture diameter.

The parameters of Table 2 are defined as follows. The first column is the parameter σ_R^2 , the spherical-wave log-amplitude Rytov variance, the second column is the parameter r_0 , the spherical-wave atmospheric coherence length (Fried parameter), and the third column is θ_0 , the isoplanatic patch angle, in microradians. D_{ap} is the aperture diameter, λ is the wavelength of the light for illumination and image formation, D_{obj} is the maximum extent of the medium-sized (80-cm long) ‘‘A’’ object, and R is the range from the object to the receiver, as noted above after Eq. (1).

Table 2. Atmospheric turbulence parameters. Parameters are defined in text.

Case	σ_R^2	r_0 (m)	θ_0 (μ rad)	D_{ap}/r_0	$\theta_0 \div (\lambda/D_{ap})$	$(D_{obj}/R) \div \theta_0$
1	10^{-4}	15.2	161	0.066	151	0.167
2	0.01	0.960	10.2	1.04	9.57	2.58
3	0.1	0.241	2.56	4.14	2.4	10.3
4	0.2	0.159	1.69	6.28	1.59	15.6
5	0.3	0.125	1.32	8.00	1.24	20.1
6	0.4	0.105	1.11	9.51	1.05	23.9
7	0.6	0.083	0.873	12.1	0.820	30.4
8	1.0	0.061	0.643	16.5	0.604	41.4
9	1.3	0.052	0.549	19.3	0.516	48.6

Three error metrics were considered. The first is the normalized cross-correlation metric, defined as

$$CX_{CORR} = \max_{\Delta i, \Delta j} \sum_{ij} O(i+\Delta i, j+\Delta j)E(i, j) / [\sum_{ij} O(i, j)^2 \sum_{ij} E(i, j)^2]^{1/2}, \quad (3)$$

where $O(i, j)$ is the diffraction-limited object at pixel (i, j) , $E(i, j)$ is the estimated object, and Δi and Δj are integers. This metric and its relation to other metrics are well-known [49-51]. CX_{CORR} is a number between 0 and 1, with values above 0.7 to 0.8 corresponding to fair or better images, based on unpublished studies with image analysts.

A second measure of image quality is the edge-spread width (EW). This particular metric does not require prior knowledge of the details of the object, except that there are edges of the object that are relatively sharp. There are several versions of this metric [52]. This particular algorithm finds the separation in pixels between 10% and 90% of maximum signal along pre-specified lines that intersect the edge of the object. Four lines are considered here. Past work indicates that 4 lines are adequate. It can be seen in Table 4 below that the edges are not sharp for the diffraction-limited objects, from review of the cases with negligible turbulence, as well as from analyses of the diffraction-limited images in Figs. 1 and 2. Another metric that is considered and used is the structural similarity metric [53], however results are not shown for this metric.

3. IMAGE RECONSTRUCTION ALGORITHMS

Both pupil-plane and focal-plane algorithms were investigated. The pupil-plane algorithms have the benefit that they are more readily applied to a synthetic-aperture approach, simply by dividing up the pupil plane into separate receivers.

On the other hand, one expects that the pupil-plane approaches will be more susceptible to anisoplanatic effects, since a single estimated wavefront for atmospheric phase can only apply to one isoplanatic patch. On the other hand, focal-plane algorithms apply to more typical imaging sensors, and are less susceptible to anisoplanatism because the short-exposure point-spread-function (PSF) maintains some general properties from one isoplanatic patch to the next (e.g., overall PSF width).

The discussion of algorithms will focus on the two focal-plane algorithms that were studied, as well as the six pupil-plane algorithms that were investigated. To preface the discussion, not all classes of algorithms were investigated. The algorithms selected for this initial effort were chosen based on their speed of execution and simplicity of implementation. More sophisticated algorithms will be investigated in future work.

The impetus for the work began with the insight that for laser speckle fields, the speckle field can be separated from the atmospheric phasors using analytic techniques as discussed in the introduction. Hence, the discussion will begin with analytic “root reconstructors.”

Analytic (Root) Reconstructors

As mentioned in the Introduction, the root reconstruction process is expected to work well when the distorting atmospheric turbulence is close to the receiver aperture. The approach described herein is a special case of [30], in which all the roots belong to one of the fields, and moreover, it is applied in the pupil plane rather than the focal plane. Focal plane approaches were described in that reference. In this case, the atmospheric phase factors out from the analytic function, and the atmosphere does not significantly distort the laser speckle field. One should also note that with a sufficiently high-order polynomial, almost any discretely-sampled function can be fit with high accuracy. Hence a key step in the analytic reconstruction process is to determine the appropriate (Nyquist) sampling of the laser speckle, and then fit that sampled field with the minimum-order polynomial. This is done with polynomials for each row in the x-direction in the pupil and then with at least one polynomial in the y-direction. Each reconstructed row has an arbitrary phase which can be estimated from polynomials in the y-direction. This results in an overall reconstruction of the complex pupil field. Since the use of one column in the y-direction is sensitive to noise, a final step involves one step of phase retrieval in which a data-based support constraint is applied. These steps are summarized in Table 3.

Table 3. Root Reconstruction Processing.

Step #	Description
1	Determine laser speckle size using autocorrelation of magnitude of laser speckle field.
2	Smooth out field irregularities due to detector noise, scintillation, and aliasing with a kernel with a width of about 10% of the speckle size estimated in Step 1.
3	Sample the laser speckle field at Nyquist. Nyquist is defined by the shortest HWHM of the autocorrelation function in the 2-D autocorrelation plane of step 1.
4	Find the best-fit complex polynomial for each row of data with the lowest possible order. The length of the rows will vary for a circular aperture.
5	Find the roots of the polynomial for each row.
6	Use the roots of the polynomial to form an estimate of the complex field corresponding to laser speckle (atmospheric phase removed).
7	Repeat steps 3-6 for at least one column of the data.
8	Correct the phasors of the rows using the longest-length estimate of the fields in columns. This is done by computing the phasor of the column field to the row field at the intersection points, and then limiting the phase to less than $\pi/2$, and applying the limited phasors to the respective rows.
9	Apply one step of phase retrieval to the resulting solution for the fields to help ensure consistency of the solution. This is done by (a) taking the Fourier Transform of the amplitude estimate to the image plane from (8), (b) applying a 5%-

	of-max-magnitude threshold in the image plane, (c) Fourier-transforming back to the pupil plane, and (d) applying the pupil aperture constraint.
--	--

A few parting comments are in order for the root reconstructors. They should be expected to work well when there are at least a few roots (zeroes) of the field in the receiver. However, in the limiting case in which the object is a point source and the received coherent field is a plane wave, there are no roots but the algorithm nonetheless performs satisfactorily, identifying the polynomial as a zeroth-order polynomial consisting of a complex constant. Further, one might expect that when the polynomials become very high order within the receiving aperture, as would arise when the mutual Fresnel number $D_{obj}D_{ap}/(\lambda R)$ of the object and the receiver is much greater than 10, the polynomials will become sensitive to small variations in the field and one might expect that the root reconstructors break down. This was also observed to be the case.

Rotational and Irrotational Phase Estimation

As mentioned above, one might speculate that the irrotational phase of the combination of laser speckle and atmospherically-induced phase would belong mostly to atmospherically-induced phase in weak to moderate turbulence. This is not the case, as demonstrated below.

The computation of irrotational phase starts with phase unwrapping [31-37]. Three different approaches to computation of the irrotational phase were investigated. The first is a least-mean-square (LMS) approach using FFT's of phase differences between neighboring points [33, 34]. A variant was used which also computes the location of branch points [34]. In the simplest version of this approach, branch cuts are straight lines between neighboring branch points of opposite polarity. The global optimization of branch cut length is computationally expensive when there are many branch points. Hence instead of global optimization, the process consists of going down a list of positive-polarity branch points and for each finding the nearest negative-polarity branch point that remains. This approximate approach clearly does not always minimize total branch cut length because positive-polarity branch points later in the list may be paired with a relatively distant, non-optimal negative polarity branch point.

The second approach for generation of rotational and irrotational phase is Goldstein's algorithm [35]. In this algorithm the rotational phase points are first identified and masked off. Then phase differences are computed and these are summed outwards from an anchor point near the middle of the aperture. Phase differences greater than π in magnitude are adjusted to $[-\pi, \pi)$. The algorithm as implemented identifies branch point locations but does not attempt to form branch cuts.

The third approach for generation of rotational and irrotational phase starts with an LMS matrix approach for unwrapping of the phase within the aperture [36, 37]. A set of global phases are applied between 0 and 2π , and phase differences are computed in both x and y directions. The global phase with the minimum overall intensity-weighted phase difference is the selected global phase. It is observed that with high-SNR measurements of the complex phase, this minimization is influenced most heavily by the lengths of the branch cuts in the aperture, so this approach minimizes the sum of the intensity-weighted cut length (IWCL) of branch cuts in the aperture in this case.

Phase Filtering of Irrotational Phase

As mentioned earlier, the separation of the unwrapped phase into irrotational and rotational components is typically not sufficient for creation of an image. This will be demonstrated in the next section. Further processing is needed to identify the atmospheric phase. The first approach attempted was to compute the phase that minimizes the difference between the true atmospheric structure function (assumed to be Kolmogorov in this case) and the estimated atmospheric component of the irrotational phase:

$$\phi(\mathbf{x}) = \operatorname{argmin} \left(\sum_{\mathbf{x}} \sum_{\Delta \mathbf{x}} \left\{ 6.88(|\Delta \mathbf{x}|/r_0)^{5/3} - [\phi(\mathbf{x}) - \phi(\mathbf{x} + \Delta \mathbf{x})] \right\}^2 \right). \quad (4)$$

One may take the derivative of the right-hand side and set it to zero to get an equation that can be applied iteratively to solve Eq. (4) for the phase. The starting point for the iteration is the irrotational phase, and the overall phase of the solution is kept fixed by

using one “anchor” phase which is set to zero. This approach computationally scales as $N^4 \cdot M$, where N is the number of sample points across the aperture and M is the number of iterations, which is also a function of N . The computational expense of this approach proved to be impractical, in part due to its slow convergence.

A second approach for phase filtering is to expand the irrotational phase in terms of Zernike polynomials. Assuming the atmospheric phase is Kolmogorov and that the strength of turbulence is known, the phase variances of the respective Zernike aberrations are also known [54]. Variances obtained from the wavefront that are too high must have contributions from laser speckle or noise. Variances that are too low imply that another source of aberration is subtracting from the atmospheric aberration. With this insight, a natural approach is simply to take the phase aberration that is within a factor of two up or down of the nominal variance for the coefficient of that Zernike aberration, and assume that it belongs to the atmospheric phase. That is, if the measured variance of the Zernike coefficient for an aberration is within a factor of two of the nominal variance, the implied coefficient is used for that Zernike aberration of atmospheric phase. If the measured variance of the Zernike coefficient is greater than a factor of two of the nominal variance, then a factor of $2^{1/2}$ is applied to the nominal coefficient for that Zernike and used. If the measured variance is less than a factor of two of the nominal variance, then a factor of $1/2^{1/2}$ is applied to the nominal coefficient of that Zernike and used. The resulting estimate of the atmospheric phase is then equal to a weighted sum of Zernike aberrations.

$$\phi_{\text{atm},e}(\mathbf{x}) = \sum_i a_i Z_i(\mathbf{x}), \quad (5)$$

where $\phi_{\text{atm},e}(\mathbf{x})$ is an estimate of the atmospheric phase, and a_i is the coefficient of the Zernike aberration $Z_i(\mathbf{x})$, determined by the process above. The choice of number of Zernike aberrations in the processing depends in part on laser speckle, but one may choose their number so that the residual atmospheric phase is less than about 1 radian for a given (known) atmospheric turbulence strength. The formula used for setting the number of Zernike polynomials is

$$N_z = \max\{5, \text{ceil}[(N\pi/4) \cdot (D_{\text{ap}}/r_0)^2]\}, \quad (6)$$

where N_z is the number of Zernikes utilized, N is a number that is user-specified, $N \approx 1$ is found to be approximately best, D_{ap} is the aperture diameter, and r_0 is the spherical-wave atmospheric coherence length as defined in Sec. 2, assumed known, at least approximately.

This estimate of the atmospheric phase is then converted to phasor form and removed from the measured pupil plane phasors, and then an image is formed digitally by reverse-propagating the field to the target plane in free space (this is accomplished by applying a correcting focus of focal length R and performing a single Fresnel propagation step).

A past study was performed [55] that showed that the variance Zernike coefficients for a spherical wave vary only weakly in moderate to strong turbulence for spherical waves (when normalized by the proper r_0) so that this approach should have some success in stronger turbulence for objects that lie within a single isoplanatic patch. For objects that occupy multiple isoplanatic patches, one would need a means to separate the pupil-plane phase arising from the different patches. In principle this could be done with an array of pinholes in focal plane, but the pinhole spacing would require variation with atmospheric conditions and the pinholes will cause loss of signal. This is especially difficult if the angular extent of the point-spread function exceeds that of the isoplanatic patch.

Branch Cut Allocation

The approaches described in the previous sections might be expected to work well in weak to moderate turbulence, but in stronger turbulence, the presence of branch points in the atmospheric phase in the pupil plane is one obstacle to better performance. To address this, one may take the approach of the previous section for the irrotational part of the atmospheric phase, and combine it with the estimates of the rotational part of the phase. However, as mentioned earlier, a means is needed to separate the zeroes of the laser speckle from the zeroes of the atmospheric phase in the pupil plane. An approach as in [30] might be adaptable to the pupil plane. One must keep in mind that the impact of atmospheric phase is no longer a simple multiplicative effect in strong

turbulence, so it is expected that the approach will not do well. As in the previous sections, a physical insight is applied. This insight, bolstered by simulation results [42], indicates that for turbulence that is not too strong, the branch points of atmospheric turbulence are relatively close together. Since branch points must emerge in pairs of opposite polarity, one expects these pairs to initially be close together. Hence, if the laser-speckle branch points are relatively well-separated, one expects a physical basis for separation might apply. More specifically, for laser speckle the density of zeros n_z is expected to be [3, Eq. 4-215]

$$n_z = \frac{\int \alpha^2 I(\alpha, \beta) d\alpha d\beta}{\int I(\alpha, \beta) d\alpha d\beta} \left[\frac{\int \beta^2 I(\alpha, \beta) d\alpha d\beta}{\int I(\alpha, \beta) d\alpha d\beta} \right]^{1/2} / (\lambda R)^2, \quad (7)$$

where $I(\alpha, \beta)$ is the radiance distribution in the object plane, λ is the wavelength of the laser light, and R is the propagation distance from object to receiver. From this, one obtains an estimate of the separation of zeroes of the laser speckle, denoted $|\Delta x_{z,ls}|$, in the pupil plane:

$$|\Delta x_{z,ls}| \equiv 1/n_z^{1/2} \sim \lambda R / [w_{obj,x} w_{obj,y}]^{1/2}, \quad (8)$$

where $w_{obj,x,y}$ are the object widths in the principal axes of the object, given by the first two terms of Eq. (7) in square brackets. For typical tactical cases of interest, R might be 1-100 km, and λ might be 1 micron. Assuming an object size of 1 meter in both axes, the resulting scale sizes for laser speckle therefore range from 3 cm to 3 meters. A 10-meter object at 100 km will have a zero separation of about 30 cm.

This estimate for the zero separation should be compared to the zero separation in weak to moderate turbulence. The scale size of zero separation from turbulence is expected to be roughly 10% of a Fresnel zone, i.e., $0.1(\lambda R)^{1/2}$ [42-43]. The resulting separation for zeros of weak-to-moderate turbulence assuming the conditions of the previous paragraph will vary from roughly 3 mm to 3 cm. Hence for these conditions, it is reasonable to expect that the zeros due to turbulence should be less than that for laser speckle. A simple rule of thumb that implements an allocation is that a pair of zeroes that are less than $0.1(\lambda z)^{1/2}$ should be applied to the atmospheric phase rather than the object's laser speckle phase for the object sizes and ranges given above.

The algorithms for computation of irrotational and rotational phase, phase filtering, and branch-cut allocation to turbulence are summarized in Table 4.

Table 4. Phase Filtering and Branch Cut Allocation.

Step #	Description
1	Measure pupil plane field phasors at a density of ~ 1 sample/cm.
2	Compute phasor differences between adjacent samples
3	Compute phase differences from phasor differences.
4	Compute irrotational phase using either (a) an LMS approach using an FFT, (b) an LMS approach using a matrix, or (c) Goldstein's algorithm.
5	Filter irrotational phase using Zernike approach to get atmospheric irrotational phase.
6	Compute local residues (local curl) of phase differences
7	Identify branch points and the polarity where magnitude of local curl is greater than $\sim \pi$.
8	Match branch points based on nearest-neighbor or intensity-weighted cut length algorithms.
9	Allocate branch points and associated branch cuts to atmospheric phase when the length is less than a specified threshold (~ 3 cm for cases considered herein).
10	Remove atmospheric phasors from measured phases.
11	Digitally form image by reverse propagation or FFT.

Generalized Expectation Maximization (GEM)

GEM is a well-known approach [38] for image reconstruction of focal-plane data. It is relatively simple and executes quickly. Experience has shown that about 70 steps are best for this type of processing. Fewer steps will not always produce good results,

and more steps will often result in over-processing of the image, resulting in added extraneous high-frequency content. Various adaptations of the basic GEM algorithm were attempted, but usually did not result in noticeably higher quality images for the data sets available. Future adaptations which was not attempted were the use of independent processing in multiple isoplanatic patches and the use of a regularization penalty function to reduce extraneous high-frequency content.

Blind-Iterative Deconvolution Variant (BID-Variant)

The approach is summarized in Table 5. Overall, the approach is of the Gerchberg-Saxton form, in which an object estimate is iteratively refined to best match the image data. A support constraint is adapted as the number of iterations is increased, eroding where little signal is present, and dilating where there is a sharp gradient in signal at an edge of the support. An intra-iteration Wiener filter is also used and adapted as the single estimated point spread function (PSF) changes from one iteration to the next. Single frame reconstructions are registered and summed incoherently. It should be noted that there are several algorithm settings that are not detailed here. These settings are fixed for the variety of cases considered here, and have not been changed since initial optimization.

The power spectral density (PSD) of the noise in the Wiener filter in Table 5 is assumed to be white. The PSD of the laser speckle noise in Table 5 is estimated of the speckle angular size in the focal plane, λ/D_{ap} :

$$PSD_{Speckle}(\mathbf{k}_\theta) = \{ 1 - \exp[-(|\mathbf{k}_\theta|^2/2)(D_{ap}/\lambda)^2] \}, \quad (9)$$

where \mathbf{k}_θ is the two-dimensional angular-frequency variable.

Table 5. BID-Variant Image Reconstruction approach.

Step #	Description
1	Begin iterative deconvolution (single frame)
2	Create initial estimate of short-exposure Point Spread Function (PSF) based on estimate of r_0 .
3	Transform object and PSF to Fourier domain
4	Construct Wiener filter in Fourier domain, $\sim FT(PSF)^*/[FT(PSF) ^2 + PSD_{Noise} + PSD_{Speckle}]$
5	Apply Wiener filter to Fourier transform of object
6	Transform object back to spatial domain
7	Apply support and positivity constraint
8	Erode support based on a threshold of near-zero values of estimate object
9	Dilate support based on sharp gradients in intensity near edge of constraint
10	Re-estimate PSF from $FT(Image_0)/\{FT[Image(n)] + PSD_{Noise}\}$
11	Estimate convergence based on fractional change of object estimate from previous step
12	If fractional change is smallest yet, save image
13	Add in a fraction of the previous image to the current image
14	Re-center working image using centroid
15	Go back to step 3 for up to 50 iterations
16	Sum (incoherently) up to N images (N=20 in this effort)

It should be clear to those skilled in the art that the above algorithms are by no means optimal. However, they will be seen to offer some benefit, even in stronger turbulence, are relatively simple, produce useful images with about 8 frames of data, and execute quickly.

4. RESULTS

The results first start with root reconstructors. Fig. 3 shows the sum of 20 registered images for the “missile” object for root reconstruction in the lower right image, 3(d), compared to no correction, in the upper left. Also for comparison a reconstruction based on removal of the irrotational phase is shown in the upper right, and that of point source phase removed (PSPR) in the lower left. The SWLA variance is 0.02 in this case. It is clear that the removal of irrotational phase by itself is not sufficient to reproduce the object. Further, the root reconstructor shows an artifact near the left tail fin of the simulated missile. This artifact goes away in weaker turbulence, but becomes dominant in stronger turbulence. The PSPR image in the lower right is relatively good, as expected in these weak turbulence conditions. Edge metrics are shown at the bottom of the respective figures and are in rough agreement with a subjective inspection of the images.

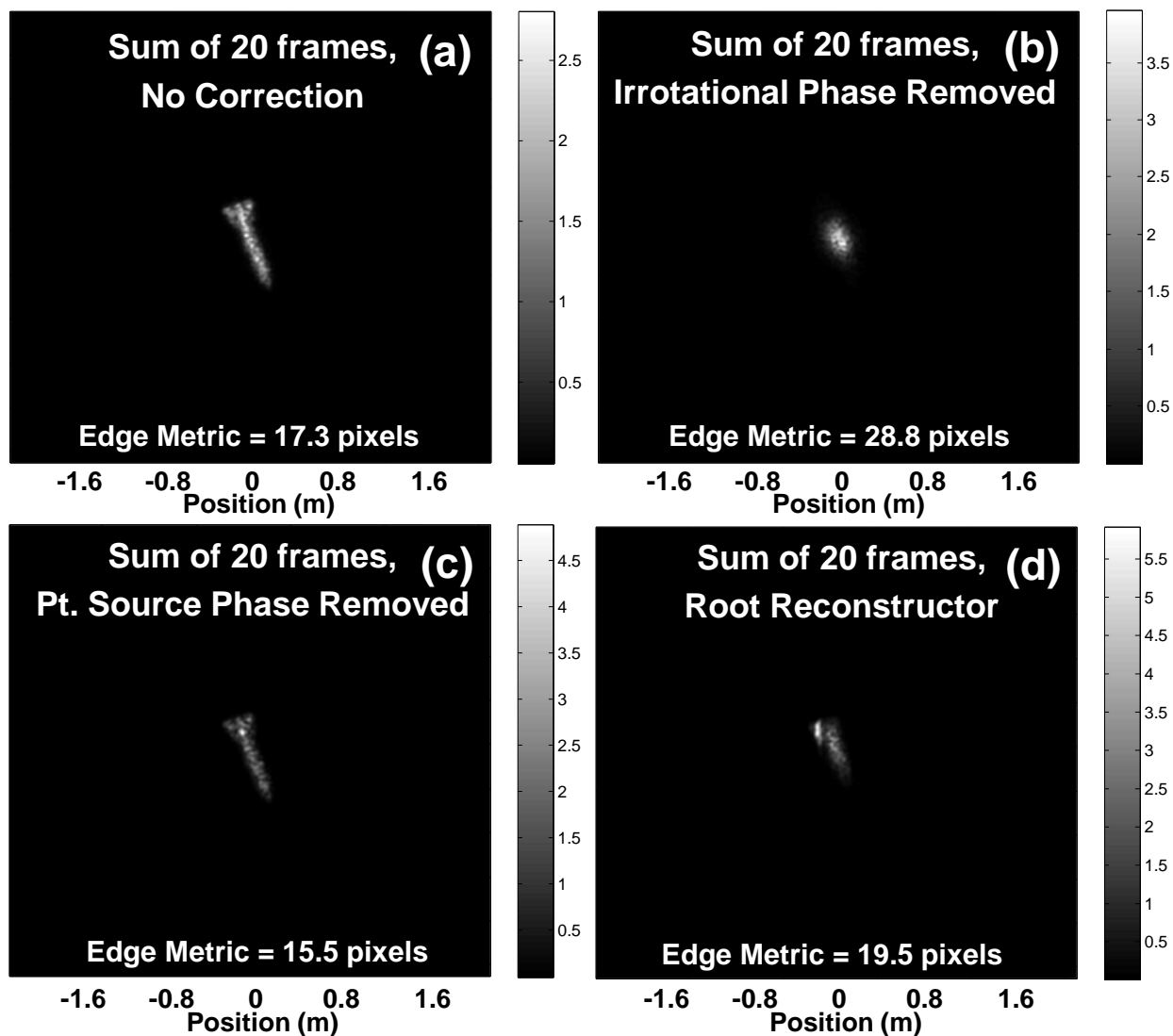


Fig. 3. Image Reconstructions of 80-cm missile object for SWLA variance of 0.02. Sum of 20 frames. (a): no correction. (b): image reconstruction by removing irrotational phase. (c): correction with point source phase removed. (d): image reconstruction using root reconstruction.

Fig. 4 shows the normalized cross-correlation ($C_{x_{corr}}$) as the number of registered and summed frames increase for the case of Fig. 3. It is seen that the no-correction case is even better than the PSPR reconstruction for these cases. Based on the frame history shown with the cyan curves, the root reconstructor evidently produces some good frames, but there are also poor frames as well.

Fig. 5 shows results for the Intensity-weighted cut length (IWCL) and Goldstein unwrapping algorithms, after Zernike filtering for a SWLA variance of 0.3 and the 80-cm “A” object. The unwrapped phases are filtered using $N=1$ in Eq. (6) for IWCL and $N=2$ for GS. The phase filtering removes most of the branch points recovered by these algorithms for this figure. The figure shows modest improvements of the algorithms compared to no correction in this case, based on both the edge metric and subjective inspection. The PSPR image shows the best qualitative improvement in this figure. Significant improvement is not expected in this case because there are so many isoplanatic patches across the object, and as mentioned earlier, a given atmospheric wavefront can only apply to one of them.

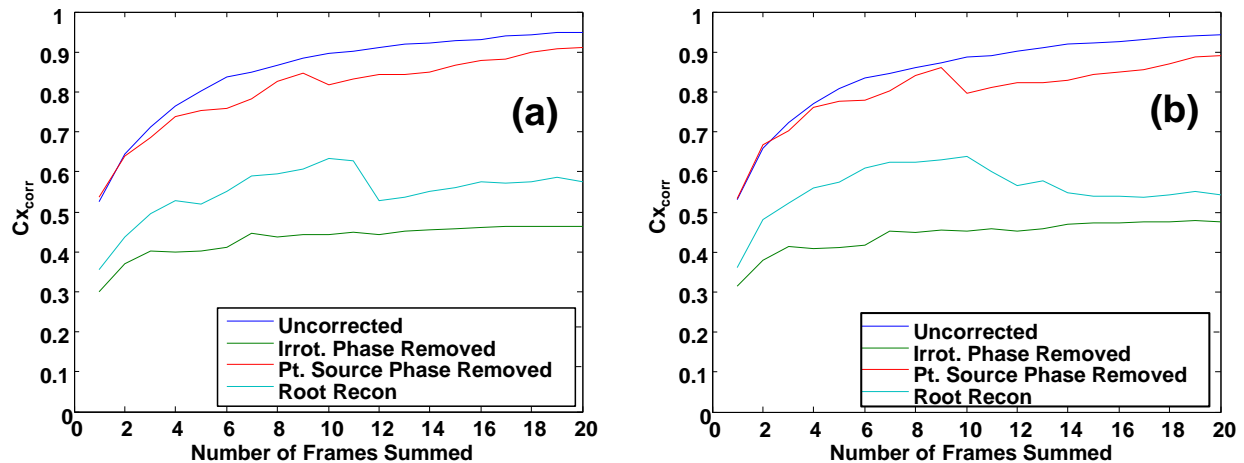


Fig. 4. Cross-correlation metric versus number of frames for cases in Fig. 3. (a) SWLA variance = 0.01. (b) SWLA variance = 0.02.

Fig. 6 shows the results corresponding to Fig. 5 for the algorithm comprising LMS phase unwrapping, phase filtering using Zernikes with $N=1$, and branch-cut allocation to atmospheric phase. The two cases shown on the left are repeats of those shown in Fig. 5, in order to facilitate side-by-side comparison. The two cases shown on the right of the figure use a branch-cut-length threshold (BCLT) of 0.9 cm and 1.8 cm for sub-figures (b) and (d) respectively. That is, for the branch cuts with length less than the stated threshold, the cuts and associated branch points are applied to the atmospheric phase. The corrected images show a very modest subjective improvement over the no-correction case. The PSPR image is subjectively the best in this figure as well.

Fig. 7 plots $C_{x_{corr}}$ versus the number of summed and registered frames for the cases corresponding to Figs. 5 and 6. On the left-hand side, subplot (a) shows plots that correspond to the cases of Fig. 5. On the right-hand side, subplot (b) shows plots corresponding to Fig. 6. Also shown in green on the left-hand side is a plot corresponding to allocation of branch cuts to atmospheric phase, for a BCLT of 1.8 cm, in order to facilitate comparison. Referring to plot (a) there are several useful observations. First, the corrected images all are better than no correction in this case. Second, the best correction is obtained with PSPR. A close second is IWCL with Zernike phase filtering, $N=1$, and not far behind are Goldstein’s algorithm with Zernike filtering, $N=2$, and LMS with Zernike filtering and branch-cut allocation. As expected from the figures, the cross-correlation metric is better than the no-correction case, but not dramatically better.

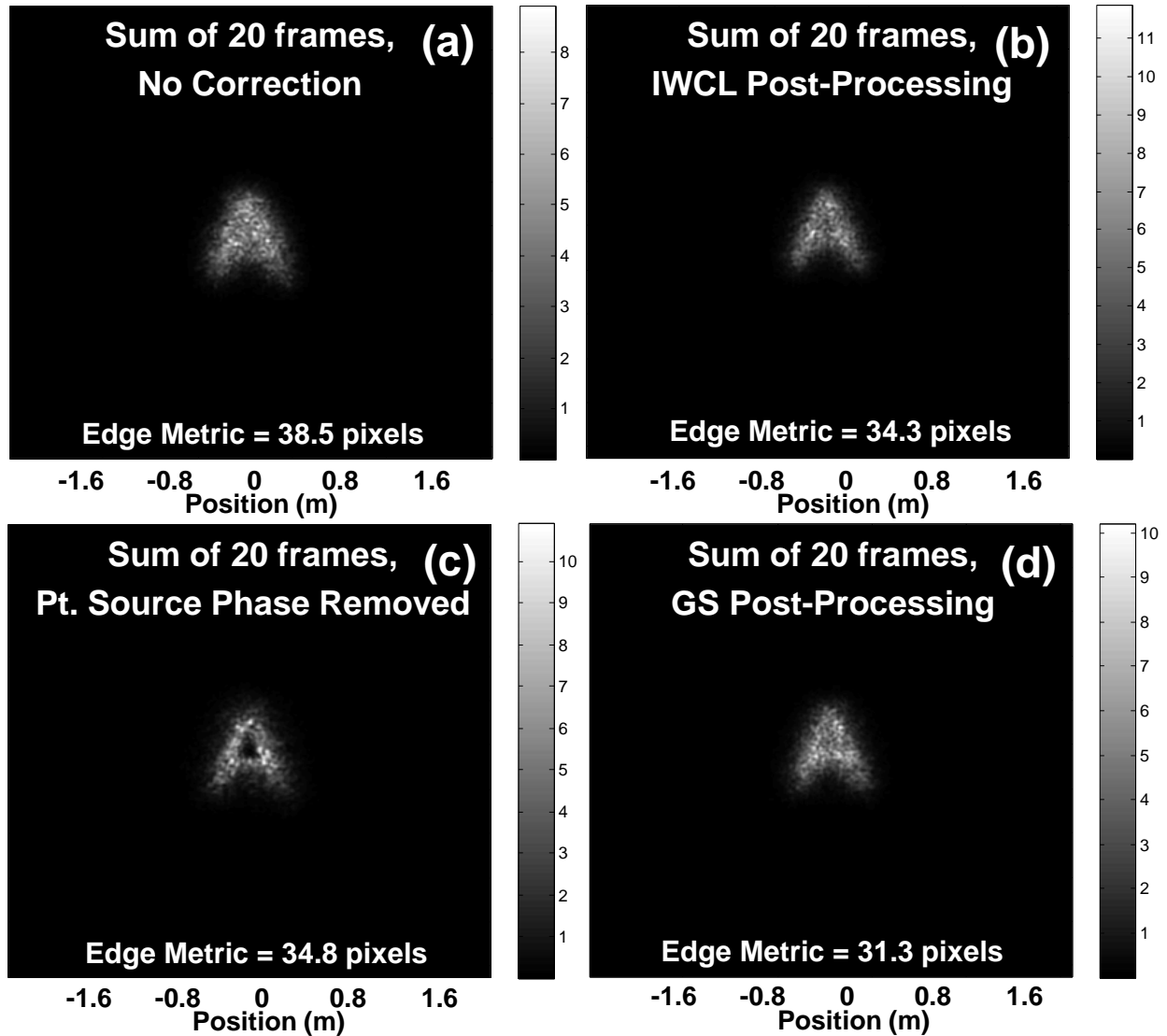


Fig. 5. Image Reconstructions of 80-cm “A” object for SWLA variance of 0.3. Sum of 20 frames. (a): no correction. (b): image reconstruction by removing Zernike-filtered IWCL irrotational phase, $N=1$. (c): correction with point source phase removed. (d): image reconstruction by removing Zernike-filtered Goldstein irrotational phase, $N=2$.

On the right-hand side of Fig. 7, subplot (b) shows results for varying thresholds for allocation of branch cuts to atmospheric phase. The bottom curve in black is for the case of a BCLT of 7.2 cm, showing the clear disadvantage of choosing a larger threshold for branch-cut allocation to the atmospheric phase. In this case, branch cuts and points associated with laser speckle are mistakenly associated with atmospheric phase. The best-performing algorithm with branch cut allocation is with the shortest BCLT, 0.9 cm. With this algorithm setting in this scenario, the performance was close to that of PSPR, shown in red.

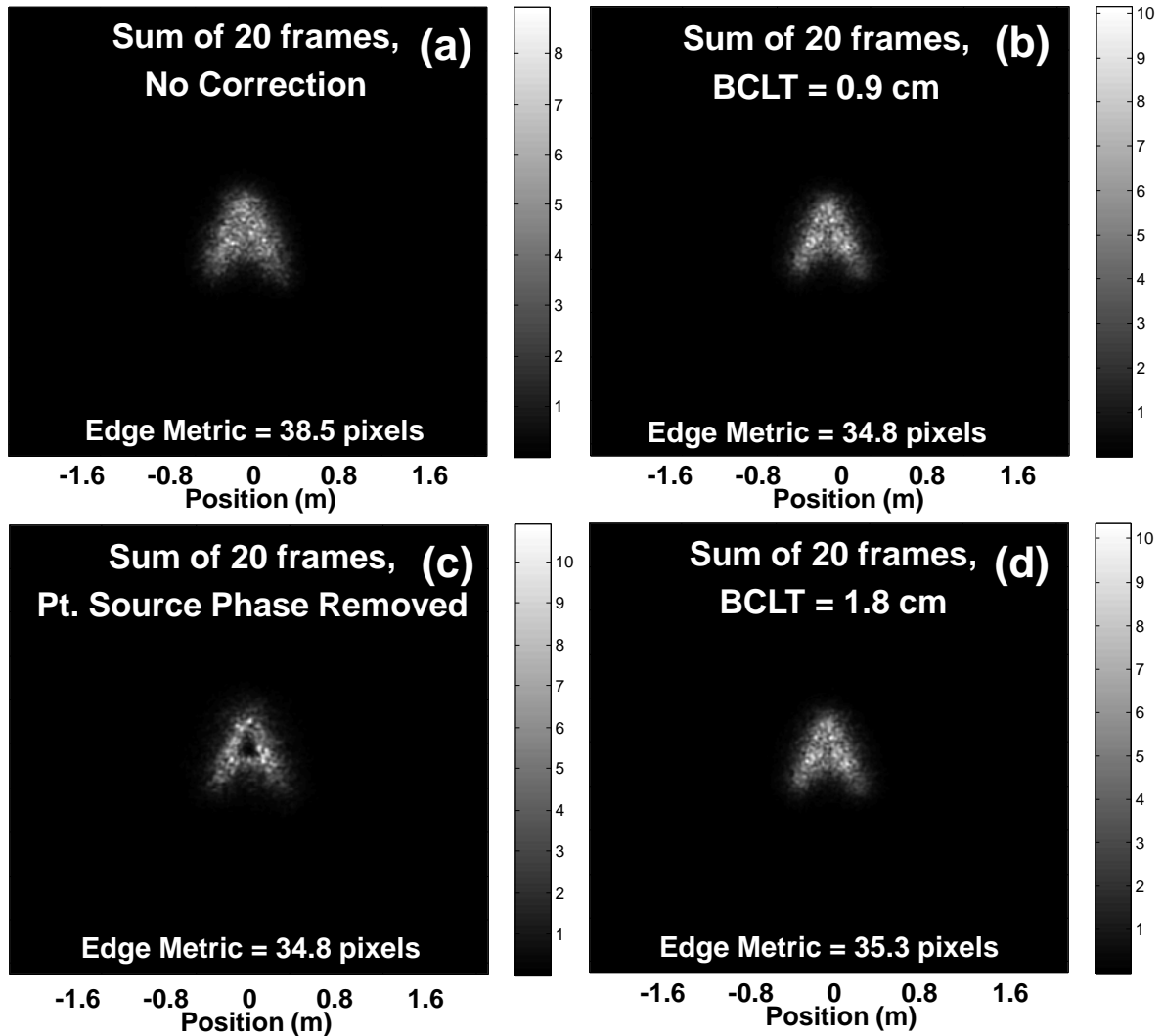


Fig. 6. Image Reconstructions of 80-cm “A” object for SWLA variance of 0.3. Sum of 20 frames. (a): no correction. (b): image reconstruction by removing Zernike-filtered LMS irrotational phase, $N=1$, $BCLT=0.9$ cm. (c): correction with point source phase removed. (d): image reconstruction by removing Zernike-filtered LMS irrotational phase, $N=1$, $BCLT=1.8$ cm.

Fig. 8 shows the cross-correlation versus number of summed and registered frames for the GEM and BID-variant algorithms. The plot on the left is for a SWLA variance of 0.4, and the plot on the right is for a SWLA variance of 1.0. In both cases, the BID-variant clearly outperforms the other algorithms as measured by $C_{X_{corr}}$, and the BID-variant is also significantly better than the no-correction case.

Fig. 9 presents results for the two focal-plane algorithms that were considered, for a SWLA variance of 0.4. Subfigure (b) shows the result for GEM, subfigure (d) shows the result for the BID-variant algorithm. In this case, the BID result is significantly better than the others as measured by the edge-width metric as well as by subjective evaluation.

Fig. 10 shows similar results for a SWLA variance of 1.0. In this case none of the algorithms give a fully-recognizable image, but the BID-variant is probably the only image that might provide an image with utility in a target-recognition paradigm, based on a subjective assessment.

It is also worth noting from Figs. 7 and 8 that most of the image-quality performance is attained with 6-8 frames of data. This corresponds to 3-4 frames of data if both polarizations of speckle from the speckle return can be utilized, and if both polarizations are statistically independent. This is a somewhat surprising result considering that past multi-frame blind deconvolution algorithms would plan to use of the order of 100 frames. However, it is less surprising in view of the theoretical result above that 1 frame of laser speckle imagery is sufficient for removal of the effects of the atmosphere in weak turbulence (albeit with speckle noise).

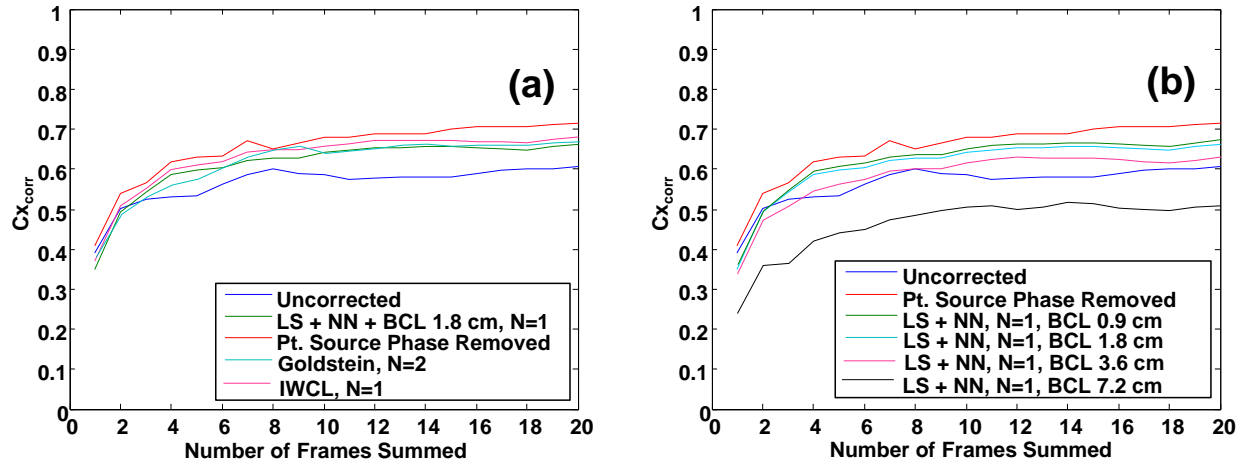


Fig. 7. Cross-correlation metric versus number of frames. SWLA variance = 0.3. (a): plots for cases of Fig. (5), as indicated in the figure legend. Also shown is LMS phase unwrapping with Zernike filtering, N=1, and allocation of branch cuts to atmospheric phase for branch-cut-lengths less than 1.8 cm, in green. (b): plots for cases of Fig. (6), as indicated in the figure legend. Also shown is LMS phase unwrapping with Zernike filtering, N=1, and allocation of branch cuts to atmospheric phase for branch-cut-lengths less than 3.6 and 7.2 cm, in magenta and black, respectively.

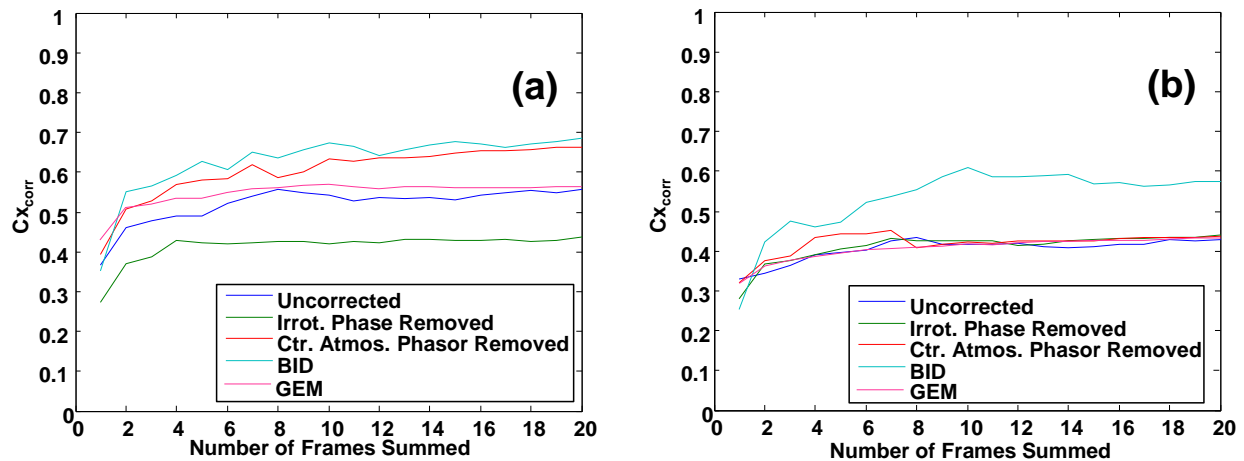


Fig. 8. Cross-correlation metric versus number of frames for Figs. 9 and 10. (a): plots for cases of Fig. (9), SWLA variance = 0.4, as indicated in the figure legend. (b): plots for cases of Fig. (10), SWLA variance = 1.0, as indicated in the figure legend.

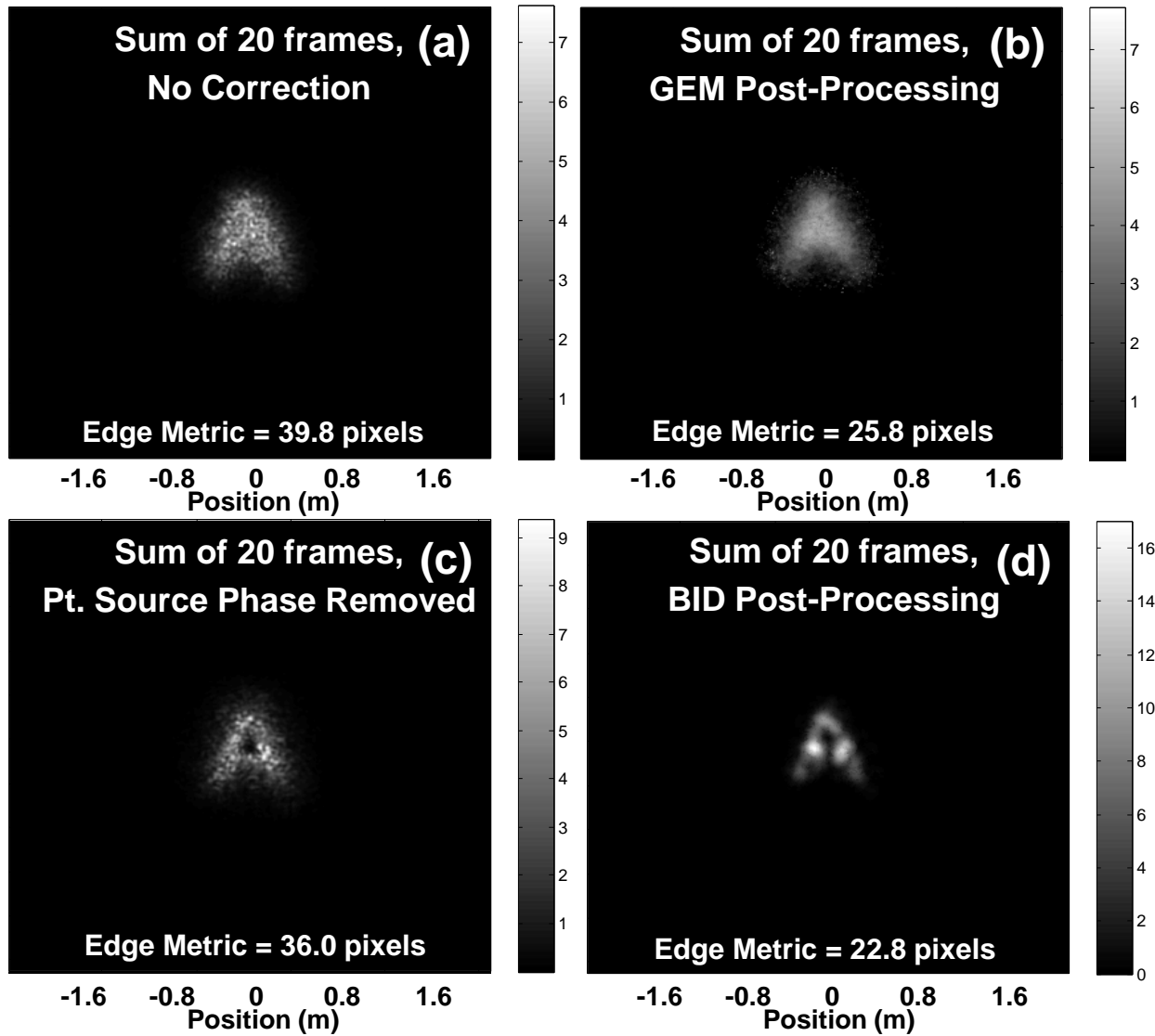


Fig. 9. Image Reconstructions of 80-cm “A” object for SWLA variance of 0.4. Sum of 20 frames. (a): no correction. (b): image reconstruction by GEM algorithm. (c): correction with point source phase removed. (d): image reconstruction using BID variant.

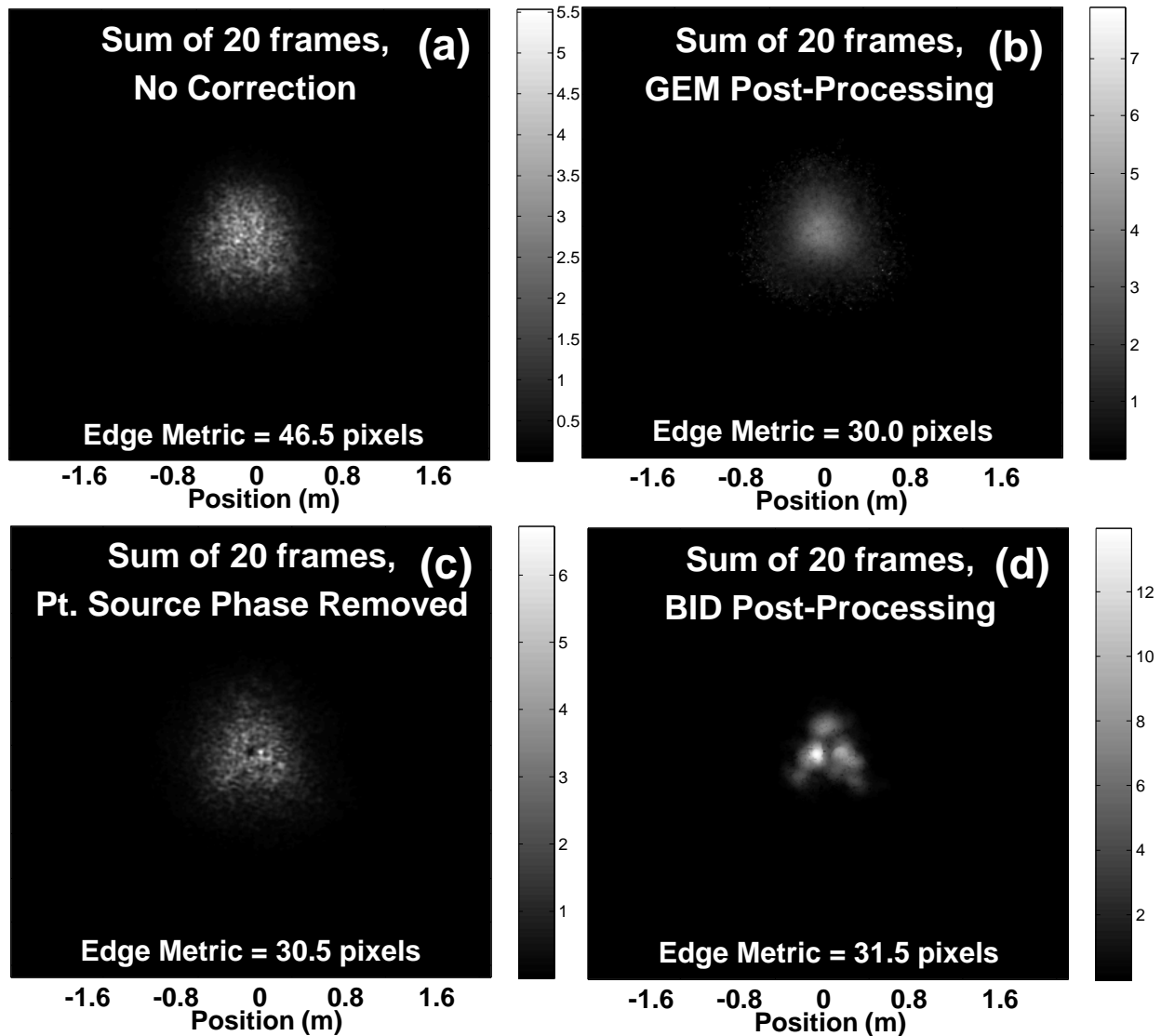


Fig. 10. Image Reconstructions of 80-cm “A” object for SWLA variance of 1.0. Sum of 20 frames. (a): no correction. (b): image reconstruction by GEM algorithm. (c): correction with point source phase removed. (d): image reconstruction using BID variant.

5. DISCUSSION AND SUMMARY

A large variety of algorithms were explored for reconstruction of images with coherent illumination in turbulence. A wave-optics simulation is used to investigate results for small, medium and large “A” and “missile” objects that are spatially bounded.

The results are prefaced by the analytic theoretical result that 1 frame of laser speckle measured in the pupil plane is sufficient for removal of the effects of the atmosphere in weak turbulence (albeit with speckle noise). The results show that the analytic approach is successful in image reconstruction for SWLA variances up to 0.02 after summing up to 20 frames of imagery.

Also shown are results for other pupil plane techniques. Pupil plane techniques have the advantage that they are compatible with synthetic-aperture approaches in which measurements can be made in small subapertures in a larger aperture, such as with a Hartmann-Shack sensor. The best pupil-plane technique tested involves removal of atmospheric phase using a single point-source incoherent beacon. The next best algorithm among the pupil plane approaches is arguably the IWCL algorithm with Zernike filtering and $N=1$. A very close third is the LMS algorithm with Zernike filtering and $N=1$, and branch-cut allocation to atmospheric turbulence when the cut is less than 0.9 cm. The algorithms showed greatest benefit over no correction in moderate turbulence (SWLA variance equal to 0.1 to about 0.3) in the scenarios considered.

The performance of pupil-plane approaches are limited by the number of isoplanatic patches across the object or scene of interest. The issue of anisoplanatism in the context of pupil-plane approaches for synthetic aperture systems has been under consideration in recent years [56]. An atmospheric phase front for one isoplanatic patch is expected to have little correlation with that of another isoplanatic patch. One could provide more point-source beacons across the object to address this. However the creation of point source beacons in specific locations on a distant object is challenging in the presence of strong or deep turbulence.

Among the two focal-plane algorithms, GEM and BID, the BID-variant did surprisingly well. Good qualitative and quantitative recognizability was maintained to a SWLA variance of 0.4, and perhaps even as high as 1.0. This is especially surprising considering that the case of SWLA variance = 0.4 corresponds to a D/r_0 of 9.5, an isoplanatic patch roughly equal to the diffraction angle λ/D_{ap} , and roughly 24 isoplanatic patches across the object. It seems incredible that one estimated PSF for the entire object could yield such a result. However, further investigation indicates that there is at least a qualitative explanation: the short-exposure PSF for each isoplanatic does have variability, but the same basic width of the PSF applies for all patches. The deviation from the average PSF (and presumably estimated) PSF is relatively small, especially after filtering out the high-frequency variations of the PSF as is done in this particular algorithm.

Further work clearly could be done. First, more objects, more ranges, and more realizations should be examined. Second, less-than-ideal sampling and more noise could be added to the simulated data. Third, non-uniform illumination could be added to the process to ascertain its impact. Fourth, more capable algorithms such as forward models could be applied to the problem. Finally, some field experiments under weak, moderate, and challenging turbulence conditions might be appropriate. Both focal-plane approaches and pupil-plane synthetic-aperture approaches have value in various applications, so both are worth further exploration.

6. ACKNOWLEDGEMENTS

The authors gratefully acknowledge that this research work was partially funded as a Laboratory Research Initiation Request by AFOSR (Air Force Office of Scientific Research) to Dr. Rao Gudimetla as principal investigator. The views expressed in this presentation are those of the authors and do not necessarily represent the views of the Department of Defense or its components.

7. REFERENCES

1. J. W. Goodman, Introduction to Fourier Optics, 2nd Ed. Section 6.5 (McGraw-Hill, New York, 1996).
2. D. R. Wehner, High Resolution Radar, 2nd ed., Chapter 6, Section 9, (Artech House, Boston, 1994).
3. J. W Goodman, Speckle Phenomena in Optics: Theory and Applications, (Roberts and Company, Englewood, Colorado, 2007).
4. J. W. Goodman, D. W. Jackson, M. Lehmann, and J. Knotts, "Experiments in Long-Distance Holographic Imagery," Appl. Opt. 8, pp. 1581-1586 (1969).

5. J. W. Goodman and R. W. Lawrence, "Digital image formation from electronically detected holograms," *Appl. Phys. Lett.* 11, pp. 77-79 (1967).
6. R. G. Paxman and J. C. Marron, "Aberration Correction of Speckled Imagery With an Image Sharpness Criterion," In *Proc. of the SPIE Conference on Statistical Optics*, 976, San Diego, CA, August (1988).
7. S. T. Thurman and J. R. Fienup, "Phase-error correction in digital holography," *J. Opt. Soc. Am. A* 25(4), pp. 983-994 (2008).
8. J. C. Marron, R. L. Kendrick, N. Seldomridge, T. D. Grow, and T. A. Höft, "Atmospheric turbulence correction using digital holographic detection: experimental results," *Opt. Express* 17, pp. 11638-11651 (2009).
9. Abbie E. Tippie and James R. Fienup, "Multiple-plane anisoplanatic phase correction in a laboratory digital holography experiment," *Opt. Lett.* 35, pp. 3291-3293 (2010).
10. P. S. Idell and J. D. Gonglewski, "Image synthesis from wavefront measurements of a coherent diffraction field," *Opt. Lett.* 15, pp. 1309-1311 (1990).
11. R. Holmes, K. Hughes, P. Fairchild, B. Spivey, and A. Smith, "Description and simulation of an active imaging technique utilizing two speckle fields: iterative reconstructors," *J. Opt. Soc. Am. A* 19, pp. 444-457 (2002).
12. T. Mavroidis, J. C. Dainty, and M. J. Northcott, "Imaging coherently illuminated objects through turbulence: plane wave illumination," *J. Opt. Soc. Am. A* 7, pp. 348-355 (1990).
13. J. W. Goodman, "Optical methods for suppressing speckle," in *Speckle Phenomena in Optics* pp. 141-186 (Roberts & Company, 2007).
14. T. S. McKechnie, "Speckle reduction," in *Laser Speckle and Related Phenomena*, J. C. Dainty, ed., pp. 123-170 (Springer, Berlin, 1975).
15. B. Redding, M.A. Choma, and H. Cao, "Speckle-free laser imaging using random laser illumination," *Nature Phot.* 6, pp. 355-359 (2012).
16. R. B. Holmes, "Mean and variance of energy reflected from a diffuse object illuminated by radiation with partial temporal coherence," *J. Opt. Soc. Am. A*, Vol. 20, pp. 1194-1200 (2003).
17. V. I. Tatarski, *Wave Propagation in a Turbulent Medium* (McGraw-Hill, New York, 1961).
18. R. L. Fante, "Electromagnetic beam propagation in turbulent media," *Proc. IEEE* 63, pp. 1669-1692 (1975).
19. L. C. Andrews and R. L. Phillips, *Laser Beam Propagation through Random Media*, 2nd ed. (SPIE, Bellingham, WA, 2005).
20. M. C. Roggemann, and B. Welsh, *Imaging Through Turbulence*, Chapter 4 (CRC Press, Boca Raton, 1996).
21. J. W. Hardy, *Adaptive Optics for Astronomical Telescopes*, 1-394 (Oxford University Press, New York, 1998).
22. R. Q. Fugate, "Adaptive Optics," Chap. 5 of *OSA Handbook of Optics, Third Edition Volume V: Atmospheric Optics, Modulators, Fiber Optics, X-Ray and Neutron Optics*, Michael Bass, ed. (McGraw-Hill, Inc. New York, NY, 2010).
23. M. I. Skolnik, *Radar Handbook*, 2nd Ed., Chapter 23, McGraw-Hill, New York, 1990.
24. R. Hudgin, "Wave-front compensation error due to finite corrector-element size," *J. Opt. Soc. Am.*, Vol. 67, pp. 393-395 (1977).
25. B. M. Levine, E. A. Martinsen, A. Wirth, A. Jankevics, M. Toledo-Quinones, F. Landers, and T. L. Bruno, "Horizontal line-of-sight turbulence over near-ground paths and implications for adaptive optics corrections in laser communications," *Appl. Opt.* 37, pp. 4553 (1998).
26. J. R. Fienup, and P.S. Idell, "Imaging correlography with sparse arrays of detectors," *Optical Engineering* 27(9), pp. 778-784 (1988).
27. J. Fienup, "Direct-detection synthetic-aperture coherent imaging by phase retrieval," *Opt. Eng.*, Vol. 56, 113111 (2017).
28. R. G. Lane and R. H. T. Bates, "Automatic multidimensional deconvolution," *J. Opt. Soc. Am. A* Vol. 4, pp. 180-188 (1987).
29. Richard Holmes, V.S. Rao Gudimetla, "Image reconstruction for coherent imaging for space surveillance and directed energy applications," *Proc. SPIE*, Vol. 9982, 99820I-10 (2016).
30. D. C. Ghiglia, L. A. Romero, and G. A. Mastin, "Systematic approach to two-dimensional blind deconvolution by zerosheet separation," *J. Opt. Soc. Am. A*, Vol. 10, pp. 1024-1036 (1993).
31. D. C. Ghiglia and M. D. Pritt, *Two-Dimensional Phase Unwrapping: Theory, Algorithms, and Software* (Wiley-Interscience, New York, 1998).
32. L. Ying, "Phase Unwrapping," *Wiley Encyclopedia of Biomedical Engineering* (Wiley, New York, 2006).
33. M. D. Pritt and J. S. Shipman, "Least-squares two-dimensional phase unwrapping using FFTs," *IEEE Trans. Geosci. Remote Sensing* 1994; 32(3):706-708.
34. G. C. Dente, M. L. Tilton, and L. J. Ulibarri, "Phase Reconstruction from Difference Equations: A Branch Point Tolerant Method," *Proc. SPIE*, Vol. 4091, pp.292-303 (2010).
35. R. M. Goldstein, H. A. Zebken, and C. L. Werner, "Satellite radar interferometry: Two-dimensional phase unwrapping," *Radio Sci.*, Vol. 23, pp. 713-720, (1988).

36. T. Venema, J. Schmidt, "Optical phase unwrapping in the presence of branch points," *Optics Express*, Vol. 16, pp. 6985-6998 (2008).
37. M. Steinbock, M. Hyde, J. Schmidt, "LPSV+7, a branch-point-tolerant reconstructor for strong turbulence adaptive optics," *Appl. Opt.*, Vol. 53, pp. 3821-3831 (2014).
38. T. J. Schulz, "Multiframe blind deconvolution of astronomical images," *J. Opt. Soc. Am. A*, vol. 10, pp. 1064-1073 (1993)
39. P. Nisenson, "Single Speckle Frame Imaging using Ayers-Dainty Blind Iterative Deconvolution," *European Southern Observatory Conference Proceedings*, 299-308 (1992).
40. R. Holmes, J. Lucas, M. Werth, V. S. R. Gudimetla, J. Riker, "Impact of Partial Spatial and Temporal Coherence on Active Track and Active Imaging," *Journal of Directed Energy*, Vol. 5, pp. 355-380 (2016).
41. V. S. Rao Gudimetla, Richard B. Holmes, James Riker, "Analytical expressions for the log-amplitude correlation function for spherical-wave propagation through anisotropic non-Kolmogorov refractive turbulence," *JOSA A* 31, pp. 148-154 (2014).
42. V. S. Gudimetla and R. Holmes, "Statistics of Branch Cut Lengths for Propagation of Coherent Fields through Turbulence," in *Imaging and Applied Optics 2017*, OSA Technical Digest (online) (Optical Society of America, 2017), paper PTh2D.1.
43. L. C. Andrews, R. L. Phillips, and C. Y. Hopen, *Laser Beam Scintillation with Applications*, page 36 (SPIE, Bellingham, 2001).
44. D. Korff, G. Dryden, R. P. Leavitt, "Isoplanicity: The translation invariance of the atmospheric Green's function" *J. Opt. Soc. Am. A*, Vol. 65, pp. 1321-1330 (1975).
45. D. L. Fried, "Anisoplanatism in adaptive optics," *J. Opt. Soc. Am.*, Vol. 72, pp. 52-61 (1982).
46. J. Stone, P. H. Hu, S. P. Mills, and S. Ma, "Anisoplanatic effects in finite-aperture optical systems," *J. Opt. Soc. Am. A*, Vol. 11, pp. 347-357 (1994).
47. R. A. Schmeltzer, "Means, variances, and covariances for laser beam propagation through a random medium," *Quart. Appl. Math.* 24, pp. 339-354 (1967).
48. D. L. Fried, "Propagation of a Spherical Wave in a Turbulent Medium," *J. Opt. Soc. Am.*, Vol. 57, pp. 175-180 (1967).
49. R. A. Muller and A. Buffington, "Real-time correction of atmospherically degraded telescope images through image sharpening," *J. Opt. Soc. Am.* 64, pp. 1200-1210 (1974).
50. Robert T. Brigantic, Michael C. Roggemann, Kenneth W. Bauer, and Byron M. Welsh, "Image-quality metrics for characterizing adaptive optics system performance," *Appl. Opt.* 36, pp. 6583-6593 (1997).
51. J. R. Fienup, "Invariant error metrics for image reconstruction," *Appl. Opt.* Vol. 36, pp. 8352-8357 (1997).
52. M. Werth, B. Calef, D. Thompson, J. Bos, S. Williams, S. Williams, "A New Performance Metric for Hybrid Adaptive Optics Systems." 2014 IEEE Aerospace Conference Proceedings (2014).
53. Z. Wang, A. C. Bovik, H. R. Sheikh, and E. P. Simoncelli, "Image Quality Assessment: From Error Visibility to Structural Similarity," *IEEE Trans. Im. Proc.*, Vol. 14, pp. 1-14 (2004).
54. R. J. Noll, "Zernike polynomials and Atmospheric Turbulence," *Jour. Opt. Soc. Am.* Vol. 66, pp. 207-211 (1976).
55. R. B. Holmes, V. S. R. Gudimetla, and M. Werth, "Zernike decomposition of aberrations in strong, anisotropic, and non-Kolmogorov atmospheric turbulence," unpublished, available upon request (2017).
56. R. Holmes, D. Gerwe, P. Idell, "Laser Phase Diversity for Beam Control in Phased Laser Arrays," U. S. Patent No. 9,541,635 (2016).